



Insights into active tectonics of eastern Taiwan from analyses of geodetic and geologic data

Wen-Jeng Huang,^{1,2} Kaj M. Johnson,¹ Jun'ichi Fukuda,^{1,3} and Shui-Beih Yu⁴

Received 11 November 2008; revised 18 August 2009; accepted 21 September 2009; published 17 March 2010.

[1] About 50 mm/yr of convergence between the Philippine Sea and Eurasian plates is absorbed in eastern Taiwan, and it remains unclear how the convergence is partitioned among active faults. The Longitudinal Valley fault (LVF), the most seismically active fault in eastern Taiwan, creeps at the surface in the south and not in the north; however, it is unclear how much of the fault is locked or creeping at depth. To address these problems, we model Holocene and interseismic deformation of elastic lithospheric blocks moving over a viscoelastic asthenosphere in eastern Taiwan. Through a fully probabilistic scheme, we invert GPS, interferometric synthetic aperture radar, creepmeter, and Holocene marine terrace data for block motions, fault slip rates, and distribution of interseismic creep. The data are explained with four blocks separated by three faults, Central Range fault, LVF, and an offshore fault. The model explains the essential features of interseismic and Holocene deformation. We find that 35–55 mm/yr of slip on the offshore fault is necessary to fit marine terrace uplift rates, which is a larger fraction of the plate convergence than previously recognized. The LVF has a Holocene slip rate of 20–30 mm/yr with approximately equal magnitudes of reverse-slip and left-lateral strike-slip components. Only about half of the surface area of the Longitudinal Valley fault appears to be locked. The southern segment of the LVF creeps at a rate of 5–28 mm/yr down to a depth of 15–20 km, while the northern segment is locked from the surface to a depth of 20 km.

Citation: Huang, W.-J., K. M. Johnson, J. Fukuda, and S.-B. Yu (2010), Insights into active tectonics of eastern Taiwan from analyses of geodetic and geologic data, *J. Geophys. Res.*, 115, B03413, doi:10.1029/2008JB006208.

1. Introduction

[2] The 150 km long Longitudinal Valley in eastern Taiwan is widely considered the active collision boundary between the Philippine Sea and Eurasian plates [Chai, 1972; Biq, 1972; Wu, 1978; Angelier *et al.*, 1986; Ho, 1986]. The valley is bounded on the east by the Longitudinal Valley fault (LVF) and on the west by the Central Range fault (CRF) (Figure 1b). The ongoing relative convergence of the two plates occurs at a rate of about 80 mm/yr in the direction of 310° [Yu *et al.*, 1997, 1999] as shown in Figure 1a. The fast collision rate has resulted in 12 large, $M > 7.0$, earthquakes since 1683 [Tsai, 1985] associated with active folds and faults located primarily at the deformation front in western Taiwan and the LVF in eastern Taiwan and perhaps the CRF and offshore fault (OSF) (Figure 1a).

[3] The seismicity rates are highest in eastern Taiwan as a result of ongoing collision of the Luzon arc with the Eurasian plate. The Longitudinal Valley fault is, in partic-

ular, highly active, with about 30% of earthquakes per year in Taiwan occurring on or near the fault [W.-S. Chen *et al.*, 2007]. Two $M \sim 7.1$ earthquake occurred near the Longitudinal Valley in 1951 (the epicenters shown in Figure 1b), generating surface rupture near the towns of Hualien, Juisui, and Chihshang (Figure 1b) [Bonilla, 1975; Cheng *et al.*, 1996]. $M \sim 6$ earthquakes are relatively frequent along the Longitudinal Valley (e.g., 2003, M 6.8, Chengkung earthquake and 2006, M 6.1, Taitung earthquake; the epicenters shown in Figure 1b). The potential for disastrous earthquakes threatens lives and facilities in the region and attracts considerable attention from Earth science communities.

[4] In order to mitigate earthquake hazard in eastern Taiwan, a number of geodetic surveys have been conducted since the early 1980s to monitor fault activity. Geodetic data include trilateration, leveling, GPS, creepmeters, and interferometric synthetic aperture radar (InSAR). The collation of these geodetic observations reveals a gradient in surface velocity of 30–40 mm/yr across the Longitudinal Valley and surface creep on the LVF between Fuyuan (23.55°N) and Luyeh (22.9°N) [Yu and Liu, 1989; Lee and Angelier, 1993; Yu and Kuo, 2001; Hsu and Bürgmann, 2006]. Figure 2 shows the GPS velocities averaged over the period 1992–1999. The gradient in horizontal velocity across the LVF zone indicates a high rate of strain accumulation. The vertical velocity field shows localized uplift in places along the trace of the LVF and subsidence of up to 15 mm/yr along the eastern coast. While there is currently subsidence along

¹Department of Geological Sciences, Indiana University, Bloomington, Indiana, USA.

²Now at Institute of Earth Sciences, Academia Sinica, Taipei, Taiwan.

³Now at Earthquake Research Institute, University of Tokyo, Tokyo, Japan.

⁴Institute of Earth Sciences, Academia Sinica, Taipei, Taiwan.

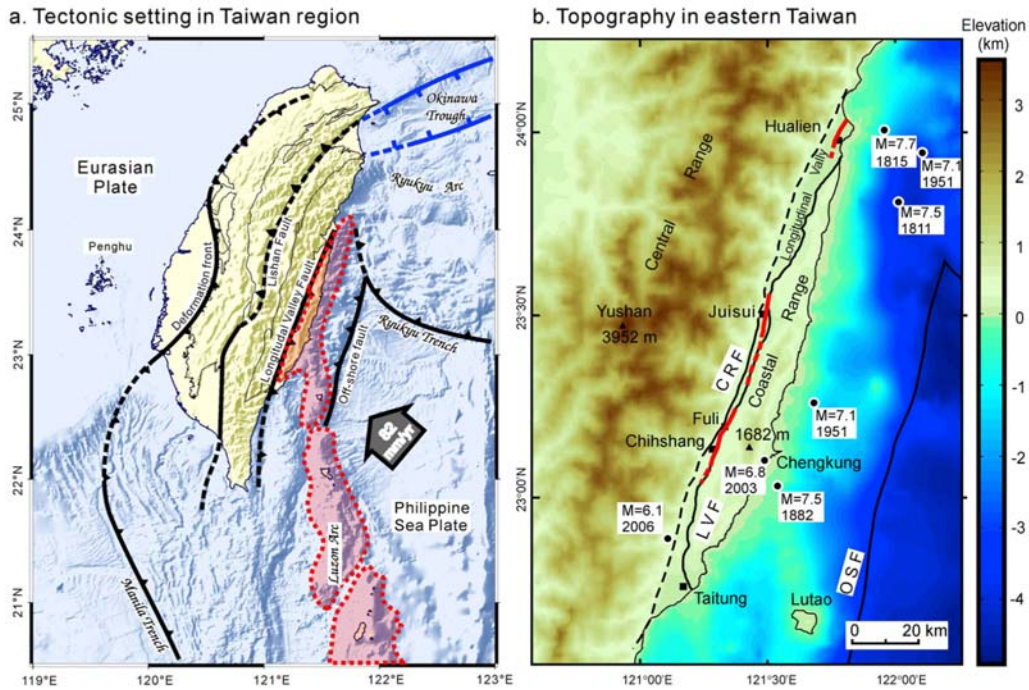


Figure 1. (a) Tectonic setting in Taiwan (modified after *Ching et al.* [2007]). (b) Topography and historical earthquakes in Hua-Tung area, eastern Taiwan. The red lines represent the surface trace of the 1951 earthquakes [*Hsu*, 1962]. CRF, Central Range fault; LVF, Longitudinal Valley fault; OSF, offshore fault.

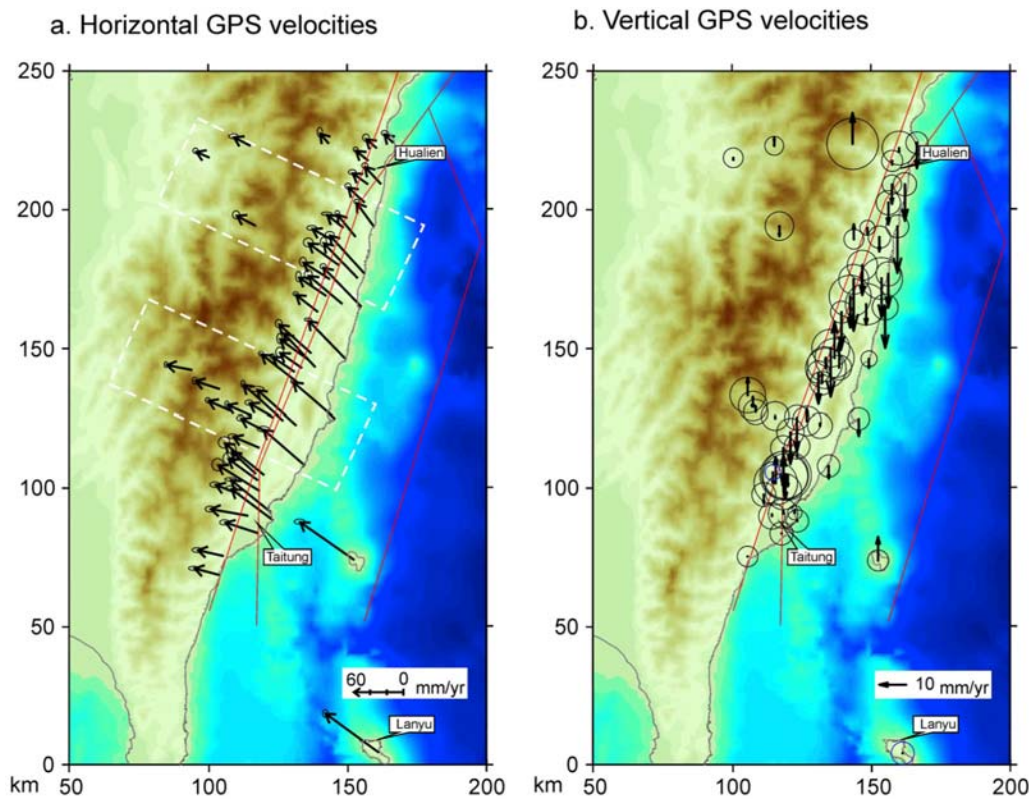


Figure 2. GPS velocities. Red lines are traces of model faults. The origin of the coordinate system is located at 22°N, 120°E (same for Figures 9, 11, 12, 13, and 14). (a) Horizontal. Ellipses are 2σ confidence regions. White dashed boxes indicate locations of two profiles in Figure 3. Only 54 sites out of 75 are shown for legibility. (b) Vertical. Circles are 2σ confidence regions. Only 57 sites out of 69 are shown for legibility.

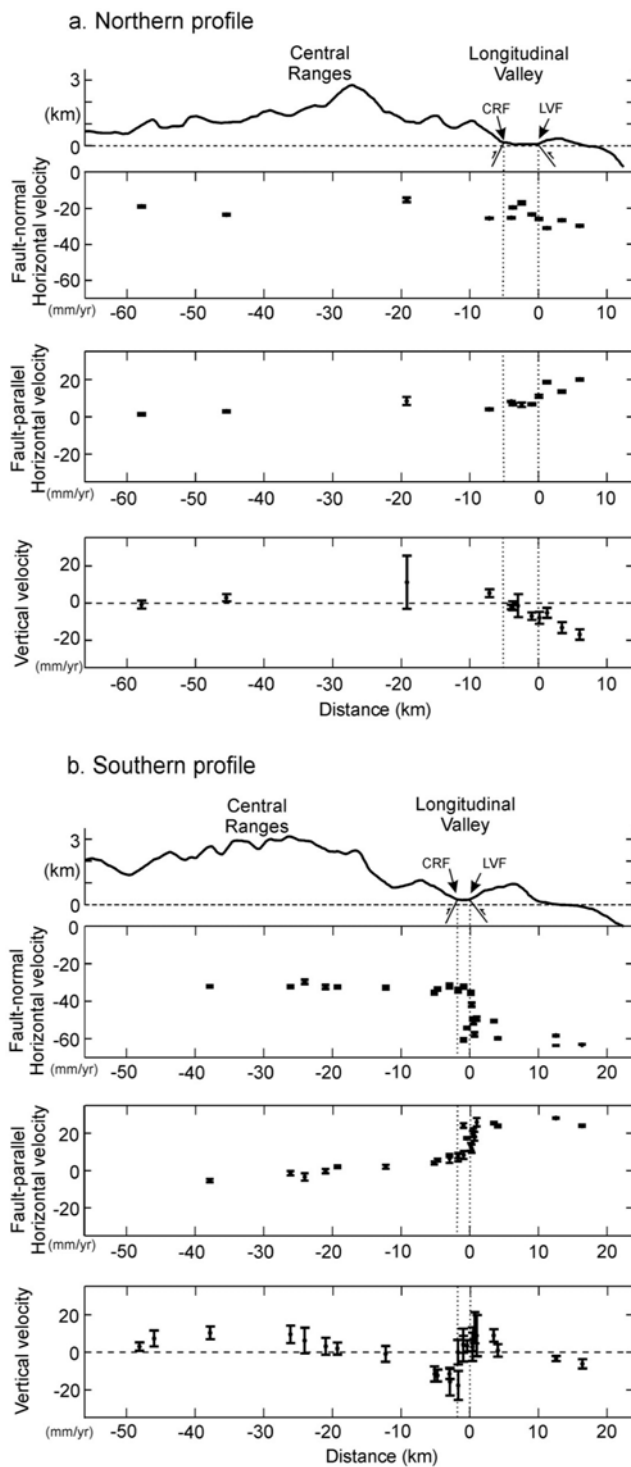


Figure 3. Profiles of GPS velocities. Dotted lines bound Longitudinal Valley (LV). (a) Northern profile. The gradient of velocities is distinct across the LV. (b) Southern profile. A step-like change in velocity appears at the surface trace of the Longitudinal Valley fault.

much of the eastern coast, this area is known to have uplifted at rates of 5–10 mm/yr over the Holocene [e.g., Wang and Burnett, 1990; Hsieh et al., 2004].

[5] There is ongoing debate regarding how much of the plate convergence is accommodated by the LVF, CRF, and

OSF. Malavieille et al. [2002] proposed that 30 mm/yr of shortening is taken up along the LVF and 17 mm/yr along the OSF based on a qualitative assessment of geodetic data [Yu et al., 1997]. In view of tectonic history, they interpreted the OSF as a primary fault and the LVF is a back thrust. Shyu et al. [2005] argued that the LVF accommodates more of the plate convergence than the OSF. Bos et al. [2003] suggested that seismicity in the offshore region near Hualien indicates slip on the offshore fault and they interpreted this slip as incipient subduction of the Philippine Sea plate under the Eurasian plate.

[6] Several studies have used geodetic data and models to estimate fault slip rates and/or fault geometry [e.g., Bos et al., 2003; Hsu et al., 2003; Johnson et al., 2005]. Bos et al. [2003] and Hsu et al. [2003] included the LVF but not CRF or OSF in their model, while Johnson et al. [2005] modeled the LVF, CRF, and OSF. Bos et al. [2003] used horizontal GPS velocities to estimate continuous deformation and/or slip rates along six major geological faults on Taiwan. Their models are purely kinematic and independent of rheology. They inferred the horizontal component of slip rate on the LVF varies from ~ 19 mm/yr at Taitung to 25 mm/yr at Yuli, and 7.8 mm/yr at Hualien. Hsu et al. [2003] used horizontal GPS velocities along profiles similar to Figure 3 to estimate the fault geometry and slip rates in the central Taiwan including the LVF. In their model, the Earth is approximated as an elastic half-space, and the surface velocity field is attributed to steady creep on buried dislocations. They inferred 28–33 mm/yr of shallow creep and 48–62 mm/yr of deep creep on the LVF. Johnson et al. [2005] adopted a viscoelastic rheology for their models and inverted both horizontal and vertical GPS velocities along profiles similar to Figure 3 using both kinematic and mechanical earthquake cycle models, and they assumed the LVF creeps at the surface. From their kinematic models they inferred slip rates on the CRF of 3–10 mm/yr in the northern profile and 25–32 mm/yr in the southern profile. The slip rates on the LVF are 46–48 mm/yr in the northern profile and 37–42 mm/yr in the southern profile. The slip rates of OSF are not significantly different from zero. In their mechanical model, they excluded CRF and OSF and inferred a steady state LVF slip rate of 50–85 mm/yr and interseismic slip rates comparable to the slip rates inferred from kinematic models. Their predicted Holocene uplift rates along the eastern coast are larger than observed by a factor of two.

[7] Current knowledge of the distribution of locked and creeping segments on the LVF are either based on or inferred from geodetic measurements. GPS and trilateration data reveal a major surface velocity discontinuity of about 30 mm/yr across the Longitudinal Valley attributed to shallow aseismic creep [Yu and Kuo, 2001]. Observable ground breakages in Chihshang are evident of fault creep on the LVF with a horizontal shortening rate of 14–27 from 1986 to 2003 as revealed from trilateration surveys and creepmeter studies [Yu et al., 1990; Angelier et al., 1997, 2000; Lee et al., 2005]. The maximum surface creep of 35 mm/yr inferred from InSAR measurements occurs along the segment between Yuli and Fuli [Hsu and Bürgmann, 2006]. However, the InSAR analysis indicated the surface creep of LVF might terminate about 10 km north of Luyeh (latitude 23.0°), whereas the trilateration and leveling networks inferred the surface creep of LVF could extended

farther south to Taitung (latitude 22.7°) [Yu *et al.*, 1990]. These observations place constraints on the along-strike extent of creep on the LVF but do not directly indicate the extent of creep at depth on the fault.

[8] In light of the various data collected and previous modeling studies, we pose two major research questions regarding how the collision between the Luzon arc on the Philippine Sea plate and the Eurasian margin is accommodated in eastern Taiwan: (1) How is the convergence partitioned between the various active faults (CRF, LVF and OSF) over Holocene? (2) Where are the active faults currently locked and building up potential for large earthquakes and where are the faults creeping?

[9] To address the above research questions, we combine various geologic and geodetic observations into a single model for interseismic deformation and longer-term, Holocene deformation. We assume faulting occurs in elastic lithospheric blocks moving over a viscoelastic asthenosphere in eastern Taiwan. We analyze the GPS horizontal and vertical velocities, InSAR-inferred vertical motion and shortening rates from creepmeters along the LVF, and Holocene uplift rates obtained from dated coastal terraces. Using these data, we estimate the spatial distribution of interseismic locked and creeping patches on faults and Holocene steady and interseismic slip rates using the hybrid kinematic-mechanical model and inversion method described by K. M. Johnson *et al.* (manuscript in preparation, 2009). We present a model for eastern Taiwan that reproduces the observed horizontal and vertical deformation patterns for both Holocene and interseismic time periods.

2. Geologic Setting

[10] Taiwan Island is located at the junction between the south facing Ryukyu arc-trench system and the west facing Luzon arc–Manila Trench (Figure 1). The two arc-trench systems separate the Philippine Sea and Eurasian plates in the east of the Central Range which straddles the island from north to south.

[11] Hsu [1976] reported the Central Range fault as a west dipping reverse fault with a high angle based on three fault-related outcrops near Chiafeng about 15 km northwest of Taitung. According to Hsu's report, one of the three outcrops exposes a high-angle reverse fault between Eocene slate of the Central Range and Pleistocene conglomerate of the Longitudinal Valley, another exposes a faulted terrace with relief of 1.5 to 2 m and the other exposes a scarplet in a terrace deposit. He also indicated the faulted terraces show the reactivation of the Central Range fault during the Quaternary. Shyu *et al.* [2006b] reported the fault has produced a number of lifted lateritic fluvial terraces along the eastern flank of the Central Range in the central reach of the Longitudinal Valley from about 40 km northeast of Chihshang to near Chihshang. According to Shyu *et al.*, the CRF appears to be an active blind fault south of Chihshang and inactive along the northern part of the valley. They also estimated a late quaternary slip rate of the fault is less than 12.8 mm/yr. Several focal mechanical solutions for the 2006 Taitung earthquake, which fell on the southern segment of the CRF, shows a fault dip of $\sim 58^\circ$ to 76° to the west [Wu *et al.*, 2006]. A similar west dipping feature is imaged in seismic profiles of the accretionary prism just south of

Taiwan [Lundberg, 2003]. Willett and Brandon [2002] and Ding *et al.* [2001] included a similar west dipping Central Range fault in numerical models of orogenic process in Taiwan. However, some studies [e.g., Crespi *et al.*, 1996; Simoes *et al.*, 2007] suggest the CRF may be an east dipping normal fault which has evolved over time probably from a back thrust [Toussaint *et al.*, 2004; Simoes *et al.*, 2007].

[12] The geometry of the Longitudinal Valley fault was inferred from relocation of earthquakes by two groups. Kuochen *et al.* [2004] relocated earthquakes to illuminate the geometry of the northern segment of LVF with strike of $N20^\circ E$ and dip of $\sim 50^\circ E$ and the geometry of the southern segment of LVF with strike $\sim N25^\circ E$ and dip $\sim 54^\circ E$. Chen and Rau [2002] relocated earthquakes to infer a listric-shaped Longitudinal Valley fault in the vicinity of the city of Taitung with dip $\sim 60^\circ$ near the ground surface and $\sim 20^\circ$ at about 25 km depth. Shyu *et al.* [2006a] estimated the LVF dip-slip rate to be $\sim 22.7 \pm 2.2$ mm/yr near the middle of the LV over the Holocene from morphotectonic investigations through a fault-bend fold model.

[13] Bathymetric relief shows the possible location of an offshore fault about 40–50 km off the east coast of Taiwan (Figure 1). Seismic reflection profiles indicate the faults are west dipping thrusts [Malavieille *et al.*, 2002]. Malavieille *et al.* [2002] hypothesized the thrust fault could accommodate about 17 mm/yr based on published geodetic data [Yu *et al.*, 1997]. Kuochen *et al.* [2004] and Bos *et al.* [2003] infer activity on the offshore fault from focal mechanism solutions and locations of microseismicity. Simoes and Avouac [2006] quantified the long-term shortening rate across the Taiwan mountain belt west of the LV to be ~ 42 mm/yr. Considering this long-term shortening rate, an estimated LVF slip rate of 23 mm/yr by Shyu *et al.* [2006a], and the total plate convergence rate [Seno *et al.*, 1993; Yu *et al.*, 1997; Sella *et al.*, 2002], Simoes and Avouac [2006] estimated that 15 to 25 mm/yr of shortening should be taken up by the OSF over the long term.

3. Data Acquisition and Analysis

3.1. GPS Velocities in Eastern Taiwan

[14] The GPS data were collected from five permanent stations and 45 epoch survey stations east of the Central Range from 1992 to 1999 [Yu and Kuo, 2001]. The velocities are shown in Figure 2 with respect to Penghu Island, located 50 km west of Taiwan on the Chinese continental margin (Figure 1a). We use horizontal GPS velocities published by Yu and Kuo [2001] and vertical GPS velocities used by Johnson *et al.* [2005]. We only use data before the 1999 Chi-Chi earthquake to avoid affects of coseismic and postseismic deformation processes. Tables S1–S5 used in this study are included in the auxiliary material.¹

3.1.1. Horizontal Velocity Field

[15] Figure 2a shows that velocities in the Longitudinal Valley between the LVF and the CRF vary from 18 to 35 mm/yr with azimuth of $283\text{--}311^\circ$ and those east of the LVF in the Coastal Range vary from 28 to 68 mm/yr with

¹Auxiliary materials are available in the HTML. doi:10.1029/2008JB006208.

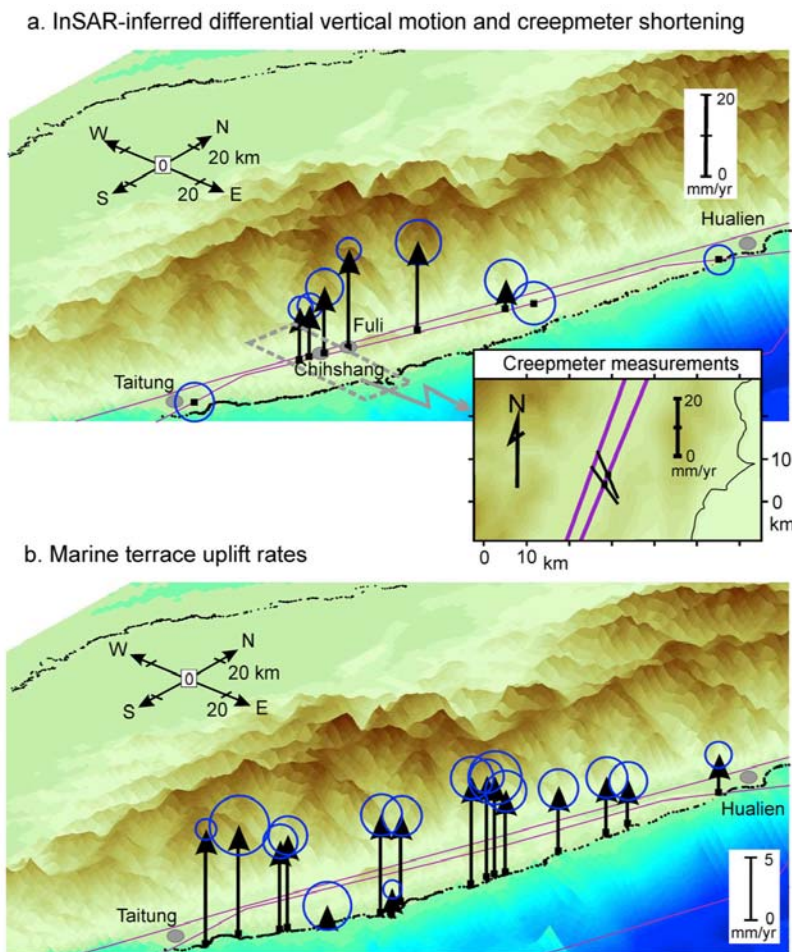


Figure 4. Geodetic and geological measurements. (a) InSAR-inferred differential vertical motion [Hsu and Bürgmann, 2006] and creepmeter shortening [Lee et al., 2001]. (b) Marine terrace uplift rates [Hsieh et al., 2004].

azimuth of $303\text{--}324^\circ$ [Yu and Kuo, 2001]. The magnitudes of the velocities decrease northwestward across the Longitudinal Valley and northeastward along the strike of the valley. The gradient of these velocities implies strain accumulation in this region. Velocities along two profiles oriented perpendicular to the regional structures in northern and southern study area are shown in Figure 3. The fault-parallel and fault-normal velocity components in both profiles show a distinct change across the LV. The salient gradient of velocities across the LV in the northern profile indicates strain is rapidly accumulating whereas the step-like velocity profile across LVF in southern profile indicates surface creep on the LVF.

3.1.2. Vertical Velocity Field

[16] Figure 2b shows the GPS vertical velocities range from 15 mm/yr of subsidence to 15 mm/yr of uplift. The areas of uplift include the southern Coastal Range, Taitung plain, and parts of the Central Range. The area of subsidence includes the northern part of the eastern coast and the northern coastal range and the entire LV and mideastern side of Central Range. The vertical GPS velocities have relatively large uncertainty as shown in Figures 2 and 3. The subsidence along the eastern coast is particularly surprising

because the direction of motion is opposite to the Holocene uplift inferred from marine terraces along the eastern coast. Examination of unpublished GPS data from continuous stations collected between 1999 and 2007 confirms the observed subsidence in the northern area of the LV.

3.2. Differential Vertical Motion and Shortening Rates Across LVF

3.2.1. InSAR Measurements

[17] We use nine measurements of differential vertical motion across the LVF ranging from 0 to 24.7 mm/yr (Figure 4) inferred from 1997 to 2000 InSAR measurements [Hsu and Bürgmann, 2006]. The spatial variation of differential vertical motion indicates surface creep on 40 km long central segment of the LVF. The maximum differential vertical motion is 24.7 mm/yr near Fuli.

3.2.2. Creepmeter Measurements

[18] We adopt two measurements of horizontal shortening rate across the southern segment of LVF shown in Figure 4a. These data indicate 19 ± 0.3 mm/yr of shortening in direction of 336° at Tapo and 17 ± 0.7 mm/yr in direction 325° at Chiyuan derived from 1 year (August 1998 to July 1999) creepmeter measurements by Lee et al. [2001]. Tapo

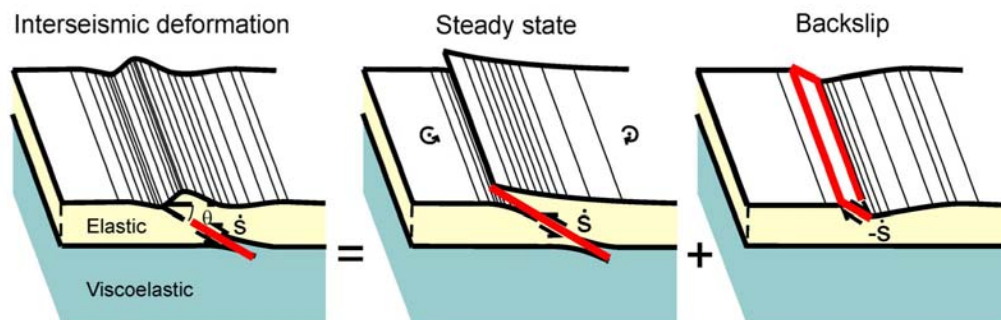


Figure 5. Illustration of lithospheric block model. Interseismic deformation is the sum of deformations for steady state and perturbation by back slip.

and Chiyuan are 2 km apart in the Chihshang area where surface breaks along the LVF are observed. Three creepmeters are located in Tapo and two are located in Chiyuan.

3.3. Eastern Coast Marine Terrace Uplift Rates

[19] Figure 4b shows uplift rates on the 140 km long eastern Hua-tung coast over the Holocene time span obtained by *Hsieh et al.* [2004] using both radiometric dating and morphological evidence. The uplift rates increase from 4 mm/yr in the north to 10 mm/yr in the south with some minor variations.

4. General Modeling Approach

4.1. Lithospheric Block Model

[20] The lithospheric block model is described in detail by K. M. Johnson et al. (manuscript in preparation, 2009). We assume that fault-bounded elastic lithospheric blocks glide over a viscoelastic asthenosphere (Figure 5). Following *Savage and Prescott* [1978] and *Savage* [1983], we decompose the deformation field into a long-term, steady component and an interseismic, transient component (Figure 5).

[21] As in the elastic block models of *McCaffrey* [2002] and *Meade and Hager* [2005], we impose a long-term,

steady velocity field such that the motion of points on blocks far from bounding faults is described by rigid-block rotation of spherical caps about a fixed Euler pole. The block motions introduce fault-parallel velocity discontinuities across bounding faults which represent the long-term, steady fault slip rates in the model. The block rotations give a purely horizontal velocity field with no vertical motion, even across dipping reverse and normal faults. We modify the block motion to account for vertical motion across dipping faults, to remove fault-normal velocity discontinuities, and to incorporate long-term distortion of blocks due to nonplanar fault geometry.

[22] The steady state surface velocity field is obtained by summing three velocity fields as illustrated in Figure 6. We begin with rotations of blocks bounded by faults defined by Euler poles of rotation. The fault-normal components of velocity discontinuities across faults are canceled by adding the velocity field generated by steady opening or closing of faults in an elastic plate. We also add a contribution to the steady state velocity field due to dip-slip motion on faults. The cancellation of fault-normal discontinuities and the contribution from dip slip is computed using the solution for a dislocation in an elastic plate overlying a relaxed viscoelastic half-space (equivalent isolated elastic plate).

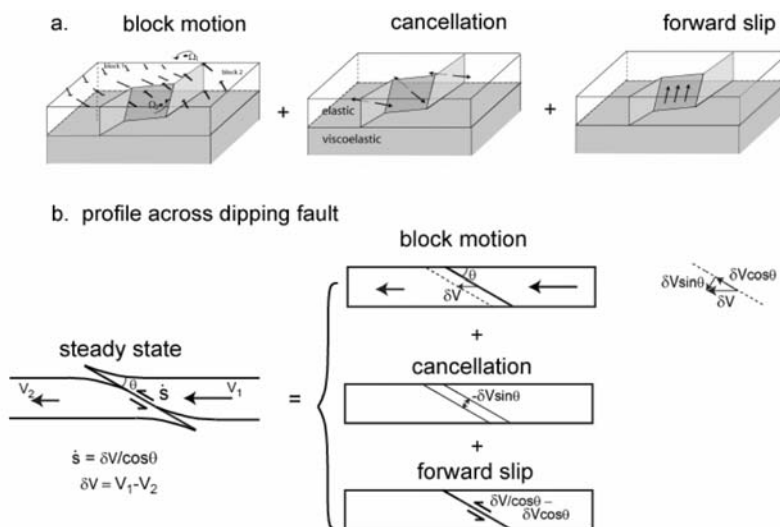


Figure 6. Illustration of steady state model construction. (a) The steady state velocity field is constructed as the sum of three velocity fields. (b) Illustration of prescribed forward slip and cancellation of fault-normal velocity discontinuity for dipping fault.

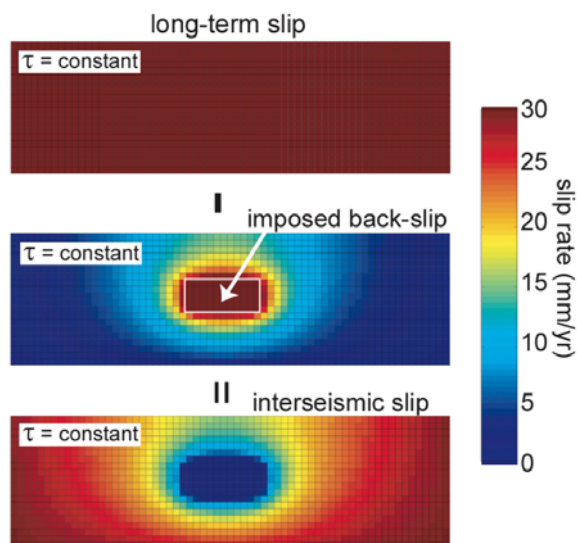


Figure 7. Construction of the model for interseismic creep. Faults are either locked (not creeping) or creeping at constant resistive stress during the interseismic period. To model creep at constant resistive stress, we superimpose steady fault slip with backward slip.

Figure 6b illustrates the model in the vicinity of a dipping fault. We assume the dip component of the slip rate is $\delta V_{\perp}/\cos(\theta)$, where $\delta V_{\perp} = V_1 - V_2$ is the horizontal component of the fault-normal velocity discontinuity and θ is the dip of the fault. This assures that the horizontal component of the velocity discontinuity across dipping faults is equal to δV_{\perp} . After cancelling the fault-normal component of the velocity discontinuity across faults, $\delta V_{\perp}\sin(\theta)$, there remains a fault-parallel component of block motion, $\delta V_{\perp}\cos(\theta)$. We therefore prescribe the full slip rate of $\delta V_{\perp}/\cos(\theta)$ by imposing steady slip on the fault of amount $\delta V_{\perp}/\cos(\theta) - \delta V_{\perp}\cos(\theta)$.

[23] The result of the summation of the three velocity fields illustrated in Figure 6 is a steady state velocity field with fault-parallel velocity discontinuities across faults and internal distortion of blocks near faults due to nonplanar fault geometry, fault-normal components of relative motion between neighboring blocks, and dip-slip motion on dipping faults.

[24] The interseismic deformation field is obtained by adding a contribution from back slip on portions of the faults that are locked during the interseismic stage. The back slip is imposed during the interseismic phase with dislocations in an elastic plate over a viscoelastic half-space at a rate that cancels the long-term slip rate imposed in the steady state model. In this paper, we consider a special case of the lithospheric block model developed by K. M. Johnson et al. (manuscript in preparation, 2009) in which the viscous relaxation time of the asthenosphere, t_R , is assumed to be long (high viscosity) relative to the repeat time, T , of earthquakes such that interseismic deformation is steady in time. In this case, back slip is modeled with dislocations in an elastic half-space. Slip on creeping patches is assumed to occur at a constant resistive shear stress (Figure 7) which is driven by imposed back slip on locked patches.

[25] Figure 7 illustrates the construction of the model for interseismic creep. We assume the creeping patches on the fault slide at constant resistive shear stress (equivalent to zero shear stress) during the interseismic period. We assume that the long-term slip determined by the steady state model described previously occurs at some constant (in time) shear stress. Fault locking is imposed by slipping locked sections of the fault backward at the long-term slip rate to completely cancel slip. Creeping areas surrounding the locked parts of the fault continue to slide at constant shear stress and therefore will also slip backward to satisfy this condition. The back slip distribution and the long-term slip rate distribution are added together to get the interseismic slip rate distribution.

4.2. Comparison With Other Models

[26] Other studies have adopted elastic half-space models to estimate fault slip rates in Taiwan. However, *Johnson et al.* [2005] showed that a lithospheric block model consisting of faulting in an elastic lithospheric plate overlying a viscous asthenosphere is more appropriate for modeling vertical motions in Taiwan. Figure 8 illustrates this point. We compare the velocity fields from the lithospheric block model to the velocity field from an elastic block model formulated by *McCaffrey* [2002] and *Meade and Hager* [2005] and that from the buried dislocation model [e.g., *Vergne et al.*, 2001; *Hsu et al.*, 2003; *Feldl and Bilham*, 2006]. The elastic block model was used by *Chuang et al.* [2008] and the buried dislocation model was used by *Hsu et al.* [2003] to model deformation over all of Taiwan. However, the elastic model didn't consider the vertical velocity field while the buried dislocation model was not able to produce satisfactory results for vertical velocities.

[27] For a simple comparison, we assume convergence across an infinitely long (along strike) reverse fault with a dip of 30° . We set up the models such that the long-term slip rate on the fault is the same in each model and the interseismic deformation field is generated by locking the entire fault down to 30 km depth. The geometry of the three models is illustrated in Figure 8a. For the lithospheric block model we use a 30 km thick elastic plate and assume that T/t_R is sufficiently small that deformation is steady in time. The elastic block model is constructed for a dipping fault using the assumption outlined by *Meade and Hager* [2005] in which far-field convergence at rate V_p is modeled with rigid-block motion and interseismic locking on the fault with dip θ is modeled with back slip at rate $V_p/\cos\theta$ on a dislocation in an elastic half-space. In the buried dislocation model, a semi-infinite horizontal detachment is placed at the bottom of the dipping fault to generate far-field convergence.

[28] Figure 8b (top) compares the lithospheric block model with the elastic block model. The horizontal velocity pattern is similar in the two models. The only difference is a small deviation from rigid block motion near the fault in the lithospheric block model due to flexure of the plate associated with slip on the fault. The vertical interseismic and long-term velocity patterns are quite different. Long-term vertical motion is assumed to be zero in the elastic block model, resulting in a nonphysical discontinuity in the interseismic vertical velocity across the fault due to the imposed back slip. The lithospheric block model assumes a discontinuity in the vertical velocity across the fault in the long term is canceled by back slip on the fault.

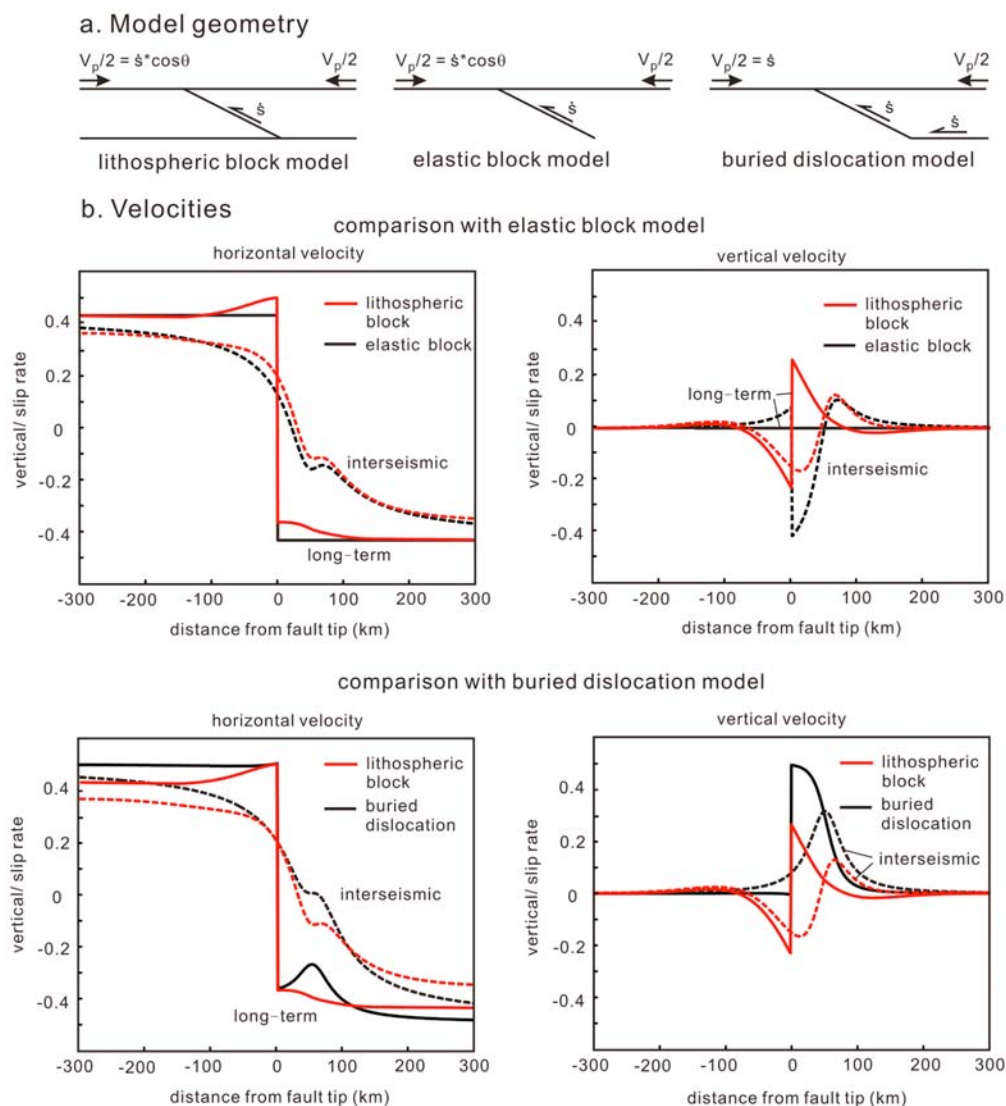


Figure 8. Comparisons between lithospheric block model, elastic block model, and buried dislocation model. (a) Model geometry. The parameter θ is fault dip. (b) Velocities from models with dip $\theta = 30^\circ$ and lithospheric thickness of 30 km.

[29] Figure 8b (bottom) compares the lithospheric block model with the buried dislocation model. The slip rate on the dipping fault in the buried dislocation model is assumed to be equal to the creep rate on the detachment to avoid a discontinuity in slip. Therefore, the convergence rate is higher in the buried dislocation model than the lithospheric block model for the same fault slip rate. This is the main difference between the horizontal velocity profiles. The vertical velocity profiles are quite different. Unlike the lithospheric block model, the buried dislocation model predicts uplift everywhere (no subsidence) and the uplift rate is higher in the buried dislocation model. The reason for the very different vertical velocity patterns is that lithospheric flexure due to thickening of the plate by thrust fault is incorporated in the lithospheric block model but is absent in the buried dislocation model. *Johnson et al.* [2005] illustrated the importance of incorporating plate flexure in models of interseismic deformation associated with reverse faults. We note that lithosphere flexure may not be an

entirely elastic process; however, the influence of plastic yielding on flexure is beyond the scope of this study.

[30] Based on the comparisons, we conclude that the lithospheric block model is the only model we have considered here that is able to provide an explanation for the interseismic subsidence and long-term uplift along the eastern coastal area. It would be inappropriate to model vertical displacements or velocities using the elastic block model. It could also be problematic to model vertical deformation using the buried dislocation model unless the effective elastic thickness of the crust is large enough to ignore the effect of plate flexure.

5. Inversion

5.1. Inversion Scheme

[31] For this problem we assume that the geometry of faults and lithosphere thickness are known but that slip rates, the distribution of locked and creeping patches, and

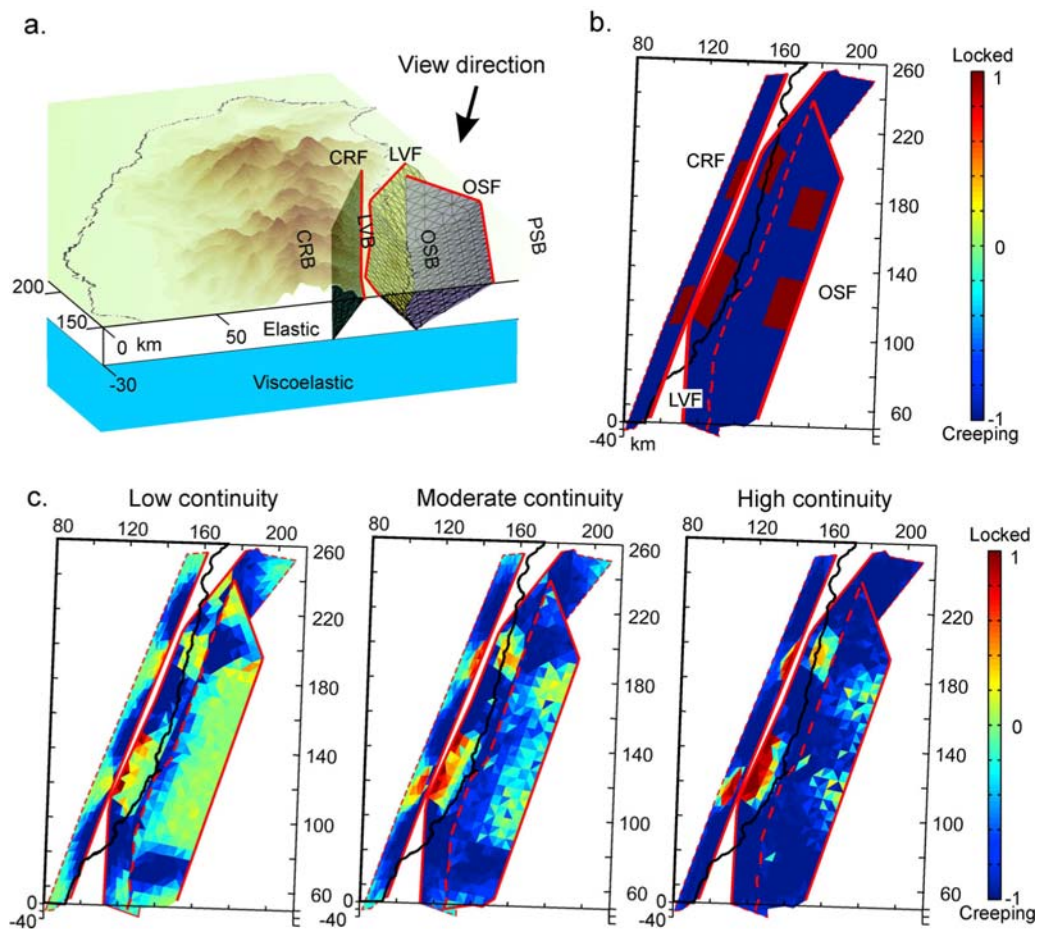


Figure 9. (a) Model geometry for eastern Taiwan. CRF, Central Range fault; LVF, Longitudinal Valley fault; OSF, offshore fault; CRB, Central Range block; LVB, Longitudinal Valley Block; OSB, offshore block; PSB, Philippine Sea Block. (b) True model for resolution test. (c) Results of resolution tests.

relative weights of disparate data sets are unknown. This results in a mixed linear/nonlinear inversion in which the components of the Euler pole vectors (which determine fault slip rates) are linearly related to surface observations and the other parameters are nonlinearly related to surface observations. To estimate the parameters, we adopt the Monte Carlo probabilistic inversion scheme of K. M. Johnson et al. (manuscript in preparation, 2009). In the method, the result of the inversion is the joint posterior probability distribution of all unknown parameters. This inverse method allows us to combine the disparate data sets with different numbers of observations and different error structures and estimate the relative weights to place on the various data sets. The inversion scheme combines the Monte Carlo-Metropolis sampling algorithm with standard analytical least squares to efficiently handle the mixed linear/nonlinear nature of the problem. In addition to the unknown model parameters, we also must specify a continuity parameter, β , which determines the relative weight placed on fitting the data versus maintaining continuity of locked and creeping patches on the fault. The continuity parameter, β , is specified rather than estimated.

5.2. Resolution Tests

[32] We conduct resolution tests to evaluate how well the distribution of locked and creeping patches is resolved with the distribution of data and the inversion scheme. In the following discussion, we refer the distribution of locked and creeping patches on faults as “patch distribution.” Because the data are concentrated between the eastern edge of the Central Range and the eastern coastline and are relatively sparse outside of this region (Figures 2 and 4), one would expect the resolution of patch distribution on the OSF and CRF to be poor. The type, number, and location of synthetic data are identical to those of the actual data but are produced by running a forward lithospheric block model with the fault geometry adopted from our analysis of real data (Figure 9a).

[33] Figure 9b shows the “true model” used to generate the synthetic data. There are two assigned locked patches on each fault. Figure 9c shows the inverted patch distribution for three different values of continuity parameter, β . The tone of the color bar at the far right represents the uncertainty of the patch distribution. Patches in colors at the ends of the color bar are fully resolved. Patches with colors in midtone of the color bar are poorly resolved. In all three cases, the creeping areas on the faults are relatively well

resolved. The locked patches on the CRF and LVF are resolved better than those on the OSF because the data are located near the CRF and LVF. The resolution of locked patches increases with increased continuity. The value for the continuity parameter has no physical meaning; we use trial and error to determine values of this continuity parameter that give results with an appreciable range in resolution.

6. Models for Eastern Taiwan

6.1. Model Setup

[34] We divide the lithosphere of eastern Taiwan into four lithospheric blocks bounded by major faults as illustrated in Figure 9a. In our analysis, we consider two models: a simple two-fault model consisting of the CRF and LVF bounding the Central Range block (CRB), Longitudinal Valley block (LVB), and Philippine Sea block (PSB) and a three-fault model including the OSF and the offshore block (OSB). We begin with the simpler two-fault model guided by the philosophy that we seek the simplest model that will account for the convergence of the Philippine Sea and Eurasian plates. Furthermore, the 2-D models of Johnson *et al.* [2005] showed insignificant contribution of the OSF to the data fitting and the resolution of the patch distribution on the OSF is poor as shown in Figure 9c. In both models we consider the motion of blocks relative to the CRB. We do not consider the motion of these blocks relative to the foothills fold-and-thrust belt farther to the west and bounded by the deformation front as shown in Figure 1a. We also do not consider the motion of the fold-and-thrust belt relative to Eurasia. Our computation of the motion of blocks relative to the CRB is valid as long as the interseismic strain associated with locking of faults at the deformation front is not captured by the GPS data (Figures 2 and 3) within the lithospheric blocks that we model. This should not be a problem considering that the deformation front is at least 100 km west of the LVF (Figure 1a) and our model domain extends no farther than 60 km west of the LVF (Figure 3).

[35] For simplicity, we specify the geometry of faults and the thickness of the elastic layer rather than estimate these parameters. The choice of fault geometry and elastic thickness is guided by geomorphologic, geological, and geophysical data. We specify a 30 km thick elastic layer, consistent with average thickness of the crust in eastern Taiwan inferred from *P* wave and *S* wave velocities [Kim *et al.*, 2005]. The model surface fault traces are shown in Figure 9. The CRF fault trace roughly follows the eastern edge of the Central Range. Following reports by Hsu [1976] and Shyu *et al.* [2006b], and considering focal mechanism solutions for the 2006 Taitung earthquake (M_w 6.1) that occurred on the southern of the CRF [e.g., Wu *et al.*, 2006] the CRF is assumed to dip 65° W. We use four segments for the LVF trace inferred from geological and geomorphic data. A dip of 50° east is assumed based on the evidence of relocated small earthquakes [Kuochen *et al.*, 2004]. Each fault segment of LVF is assumed to have a uniform dip with depth; for simplicity we do not simulate the listric shape of the LVF fault in the southern region of our study area as imaged by the relocated small earthquakes [Chen and Rau, 2002; Kuochen *et al.*, 2004]. We adopt two fault segments for OSF with the location of the traces coincident with

distinct breaks in bathymetric relief. We specified a fault dip of 30° west based on shallow seismic reflection images [Malavieille *et al.*, 2002, Figure 14].

[36] Because there are few data to constrain the slip rate on the CRF, we place a loose Gaussian prior probability distribution with mean of 12.8 mm/yr and standard deviation of 6.4 mm/yr on the CRF for the long-term dip-slip component based on the study of Shyu *et al.* [2006b]. Also, because there are few velocity vectors to constrain the motion of the Philippine Sea plate, we add a “pseudo datum” at 123°E , $23^\circ45'\text{N}$ of the same magnitude, orientation, and uncertainty as the measurement at Lanyu islet (location shown in Figure 1b). The Lanyu islet is located offshore in the southeastern corner of our study area on the Philippine Sea plate and the pseudo point is located northeast of the study area on the Philippine Sea plate. The ‘pseudo datum’ better constrains the northwestward motion of the northern part of the Philippine Sea block in our models at a rate of ~ 80 mm/yr relative to the Eurasian continental shelf.

[37] We further neglect deformation associated with interseismic locking of the subduction interface at the Ryukyu trench (Figure 1a). As indicated by the dashed line in Figure 1a, the geometry of the trench is unclear at the western end near the island of Taiwan.

6.2. Results

6.2.1. Two-Fault Model

[38] Figure 10 shows the estimated Holocene fault slip rates on the LVF and CRF. The slip rate on the LVF ranges from 55 to 90 mm/yr. The sense of slip on the LVF is oblique reverse with a small left-lateral strike-slip component. The slip rate on the CRF is about 13 mm/yr with reverse sense. We find that the predicted Holocene fault slip rates are nearly insensitive to the choice continuity parameter, β . The fit to the GPS and marine terrace data is shown in Figure 11. Although the GPS data are largely fit within the 2σ uncertainties, the downfall of the two-fault model is the overprediction of Holocene uplift rates on the eastern coast (Figure 11c). The predicted uplift rates of 25 to 50 mm/yr are 2–10 times larger than the uplift rates of 5–10 mm/yr inferred by Hsieh *et al.* [2004]. Because the predicted Holocene coastal uplift rate is proportional to the slip rate on the LVF, it is clear from the large misfits that the estimated Holocene fault slip rate on the LVF is much too high. The predicted coastal uplift rate will also depend on the choice of elastic thickness and dip of the LVF. However, we examined a range of values for these parameters and found all models over predict the coastal uplift rates.

[39] One way to reduce the slip rate on the LVF and still accommodated the ~ 50 mm/yr of relative convergence between the PSB and CRB is to accommodate a portion of the convergence offshore. Next we consider a model that includes the OSF.

6.2.2. Three-Fault Model

[40] The data fits for the three-fault model are shown in Figure 12. The predictions are consistent with the first-order patterns of these measurements. In particular, the predicted Holocene uplift rates along the coast decrease dramatically from the predicted uplift rates of the two-fault model shown in Figure 11 and match the observed data well. The fit to the

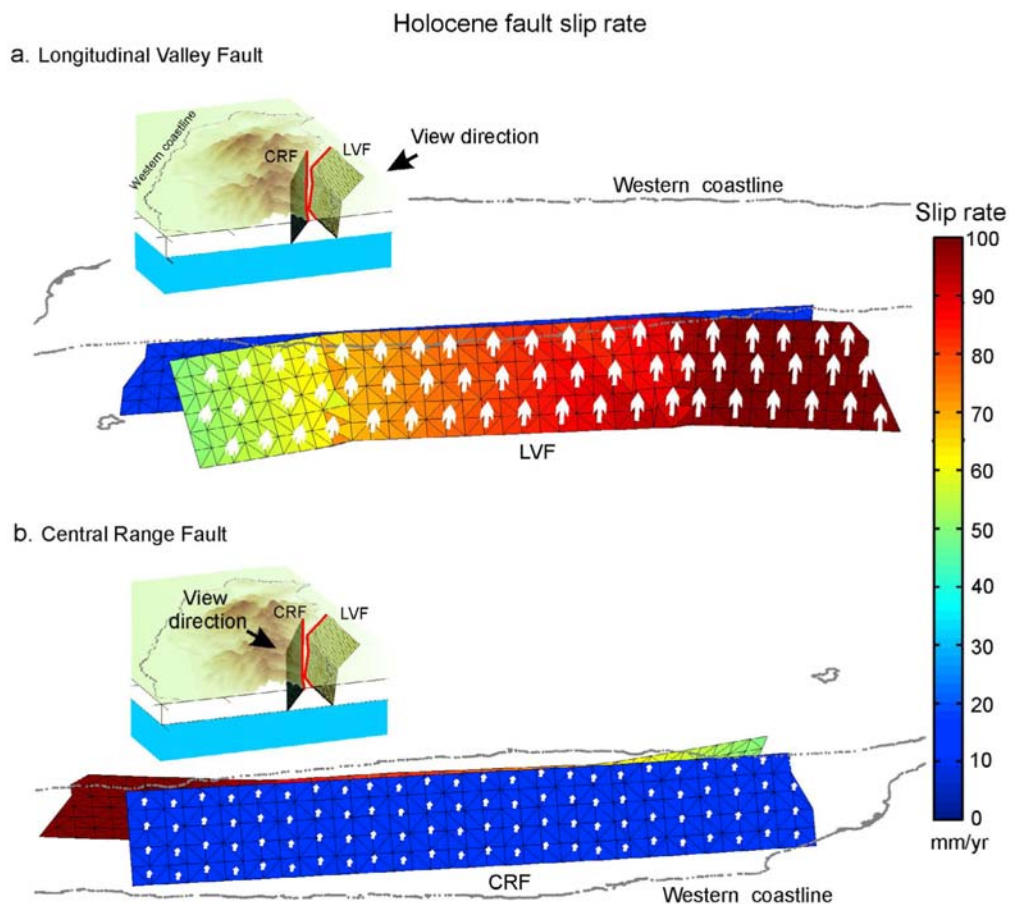


Figure 10. Estimated Holocene slip rate vectors on faults using two-fault lithospheric block model. (a) Longitudinal Valley fault (LVF). (b) Central Range fault (CRF).

horizontal GPS velocities is quite good in the region east of the LVF shown in Figure 12a. There is a systematic velocity residual of 10–15 mm/yr along the eastern coast that is likely due to mismodeled geometry of the OSF or LVF. The velocity residual for the westernmost two stations is relatively larger than others west of the CRF. This may be attributed to the influence of interseismic loading of faults in the western foothills [Loevenbruck *et al.*, 2001; Hsu *et al.*, 2003; Dominguez *et al.*, 2003; Johnson *et al.*, 2005], which is not modeled in this study. The pattern of the GPS vertical velocity field is matched well in Figure 12b. The predicted result shows subsidence in the northern coastal area and uplift along the creeping section of the LVF. The maximum predicted relative uplift along the LVF is 16.4 mm/y which is about 8 mm/yr smaller than the InSAR-inferred uplift rates, however the pattern and lateral extent of predicted uplift is similar to the InSAR data in Figure 12c. The fit to creepmeter measurements is good as shown in Figure 12d.

[41] Figure 13b shows the estimated Holocene fault slip rates. In the following discussion, all cited ranges of slip rates are 95% confidence ranges. On the upper segment of the LVF (above the intersection with the OSF), the slip rate decreases from 25 to 35 mm/yr in the south to 12–28 mm/yr in the north. The fault slip consists of approximately equal components reverse- and left-lateral strike slip. On the OSF, the fault slip rate increases from 27 to 43 mm/yr in the south

to 48–62 mm/yr in the north. The sense of fault slip is oblique reverse with a small left-lateral strike-slip component. The fault slip rate on the CRF is about 10.1–14.1 mm/yr with reverse sense. In comparison with the two-fault model in Figure 10a, the fault slip rate on the LVF at shallow depth drops significantly after adding the OSF because in the three-fault model the convergence between the Philippine Sea plate and Taiwan is partitioned between two faults. The fault slip rate on the part of the LVF below the OSF, which is essentially the sum of the upper LVF and OSF slip rates, ranges from 50 to 90 mm/yr and is nearly identical to the LVF slip rate in the two-fault model as shown Figure 10a.

[42] Figures 13a and 13c show the estimated patch distribution and interseismic slip rate, respectively. The on-land northern segment of LVF is locked whereas the on-land southern segment is creeping from 5 to 28 mm/yr. The CRF is almost entirely creeping at the long-term rate of about 12 mm/yr except for the far southern segment which is locked. The northern segment of the OSF is creeping at a rate of 15 to 45 mm/yr while most of the southern segment of OSF is locked. However, data is sparse on the hanging wall side of the CRF and there is only one measurement offshore, so the inferred distribution of creep on the CRF and OSF should be viewed with skepticism.

[43] Although this model explains the deformation for Holocene and short-term periods well, we have not modeled

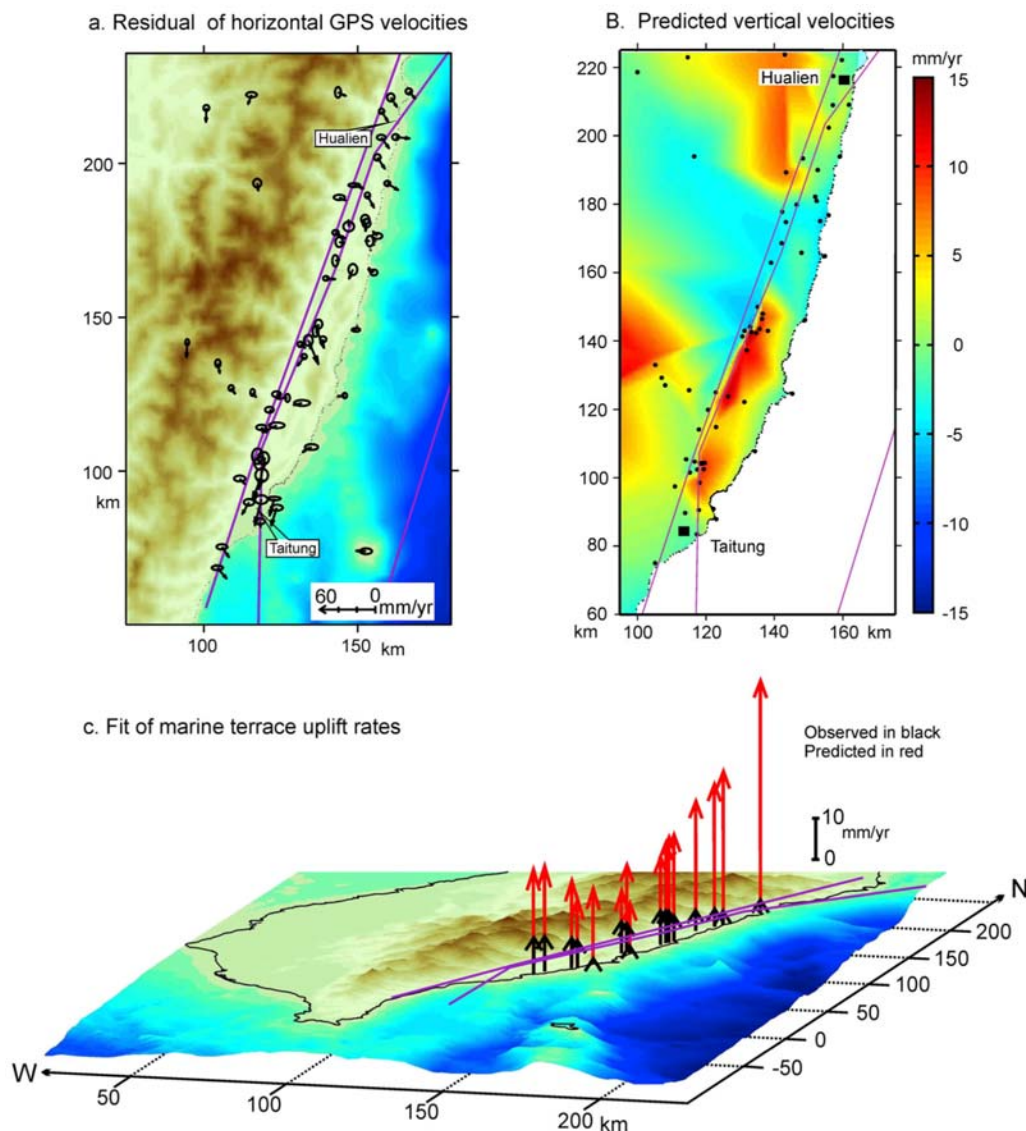


Figure 11. Results from two-fault model. (a) Residual of horizontal GPS velocities. (b) Predicted vertical velocities. (c) Coastal uplift rates.

deformation sources that may be associated with uplift and exhumation of the Central Range. For example, *Simoes et al.* [2007] invoked an underplating mechanism for uplift of the Central Range. Certainly active underplating under the CR could lead to broad-scale uplift, including uplift of the coastal ranges. If this mechanism is responsible for uplift of the coast, then the logical consequence is that our Holocene slip rate estimate for the LVF would have to be further reduced, which would require even more slip on the offshore fault. We cannot quantify this because we have not modeled the broad-scale underplating effect.

7. Discussion

[44] Figure 14 shows surface ruptures from the 1951 earthquake sequence and the estimated slip deficit per year (Holocene slip rate minus interseismic slip rate) on the upper segment of the LVF from the three-fault model. The series of 1951 Hualien-Taitung earthquakes included two

earthquakes of magnitude ~ 7.1 on 22 October and 24 November [Hsu, 1955, 1962; Bonilla, 1975; Cheng et al., 1996]. According to Hsu [1962], a 7 km wide earthquake rupture appeared near Hualien on 22 October and another two longer earthquake ruptures appeared in the central Longitudinal Valley on 24 November as shown in Figure 14. We have interpreted Hsu's solid lines as indicating known ruptures and Hsu's dashed lines as indicating uncertain rupture locations. The maximum reported displacements in the 22 October rupture were 2 m of left-lateral slip and 1.2 m uplift of southeastern side of the rupture somewhere near Hualien. The maximum displacements reported for the 25 November 1951 rupture at Juisui were 1.63 m left slip and 1.3 m of uplift of the east side of the trace [Hsu, 1955, 1962; Bonilla, 1975]. These two locations of reported maximum displacement correspond with locations of high slip rate deficit along the LVF surface trace in our model (Figure 14).

[45] Bonilla [1975] attained a left oblique slip of 2.3 m for the 22 October rupture near Hualien, assuming that the

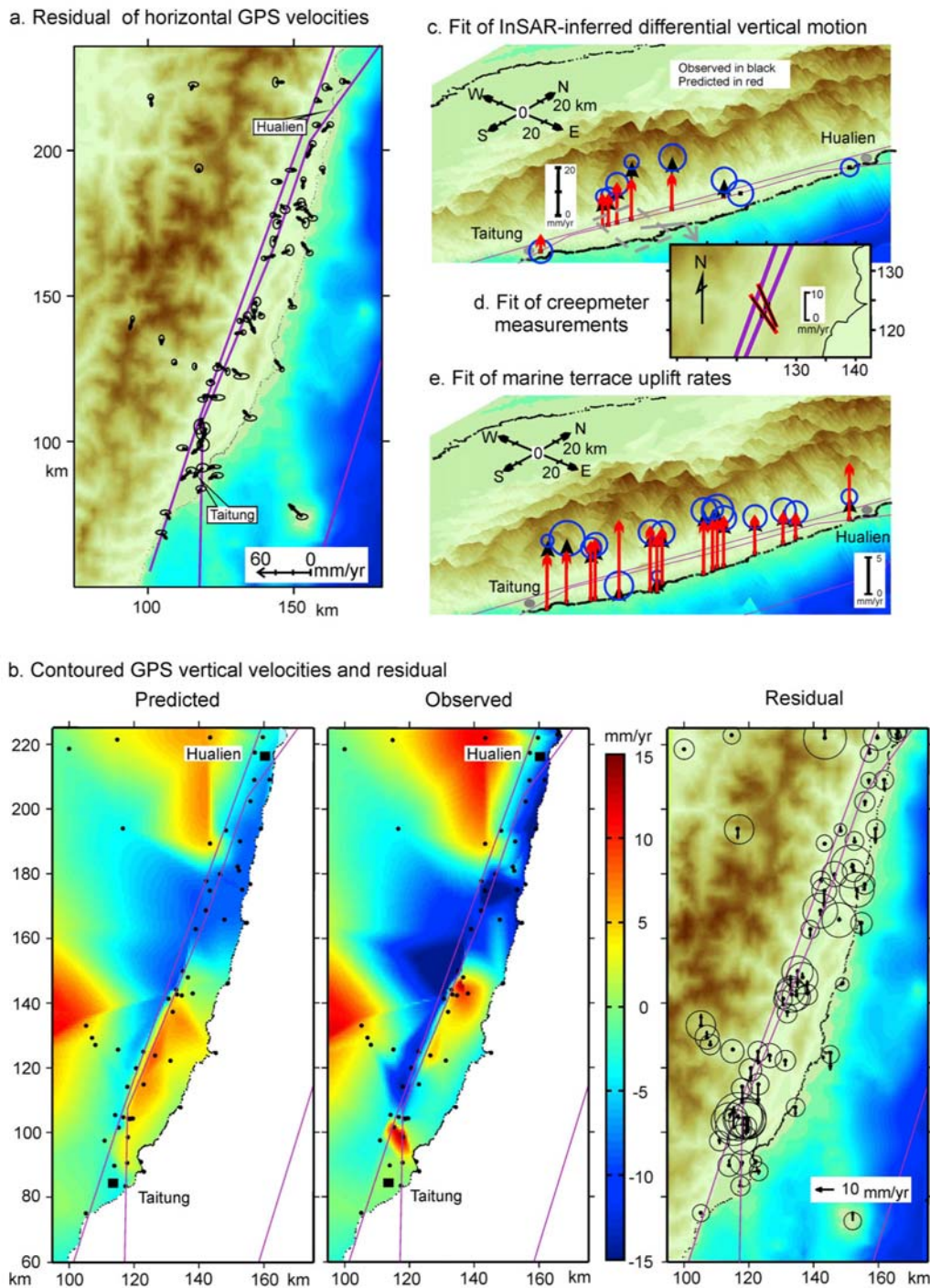


Figure 12. Comparison of observations and model predictions. (a) Horizontal GPS velocities. (b) Vertical GPS velocities. (c) InSAR-inferred differential vertical motion. (d) Creepmeter measurements. (e) Marine terrace uplift rates.

maximum horizontal and vertical components of displacement occurred at the same place. From our model, we estimate at least 90 years to accumulate this amount of slip. For the 25 November rupture, the maximum vertical and horizontal displacement were measured at the sample place northeast Juisui [Hsu, 1962] and yield a left oblique slip of 2.08 m [Bonilla, 1975]. We estimate at least 80 years to accumulate this slip. Paleoseismic studies on three

excavations across the Longitudinal Valley fault in Juisui indicate an earthquake recurrence interval of about 170–210 years since about 700 years ago [W.-S. Chen *et al.*, 2007]. From our model, we estimate ~ 4.3 to 5.3 m of slip deficit over this interval which is about twice as large as the maximum slip measured at the ground surface in 1951. However, caution is needed when interpreting surface slip measurements across ground ruptures because it has been

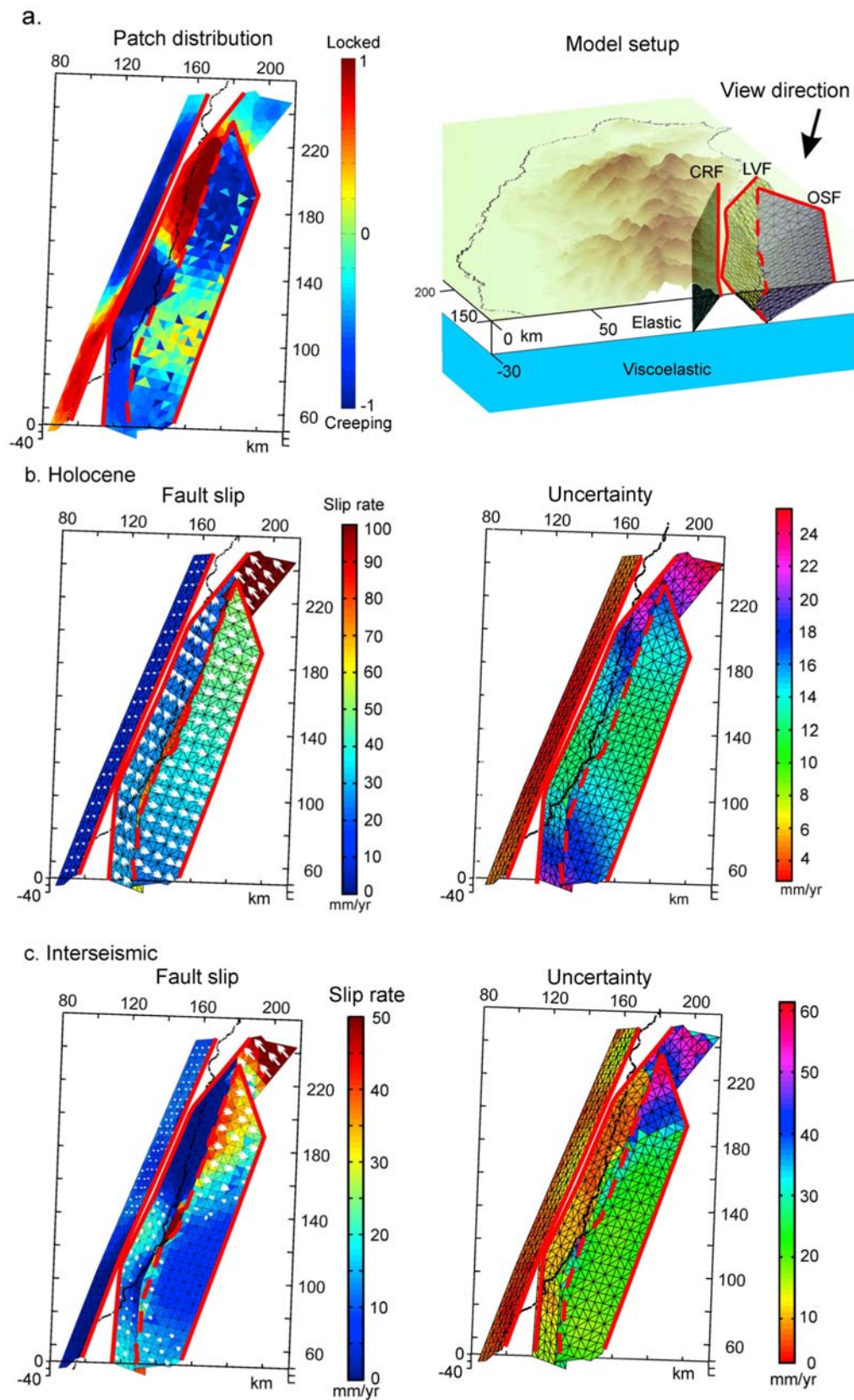


Figure 13. Results from three-fault model. Red solid lines are fault surface traces. Red dashed line is intersection of LVF and OSF. (a) Distribution of (left) locked and creeping patches and (right) model geometry. (b) (left) Holocene fault slip rates and (right) uncertainties. (c) (left) Interseismic slip rates and (right) uncertainties.

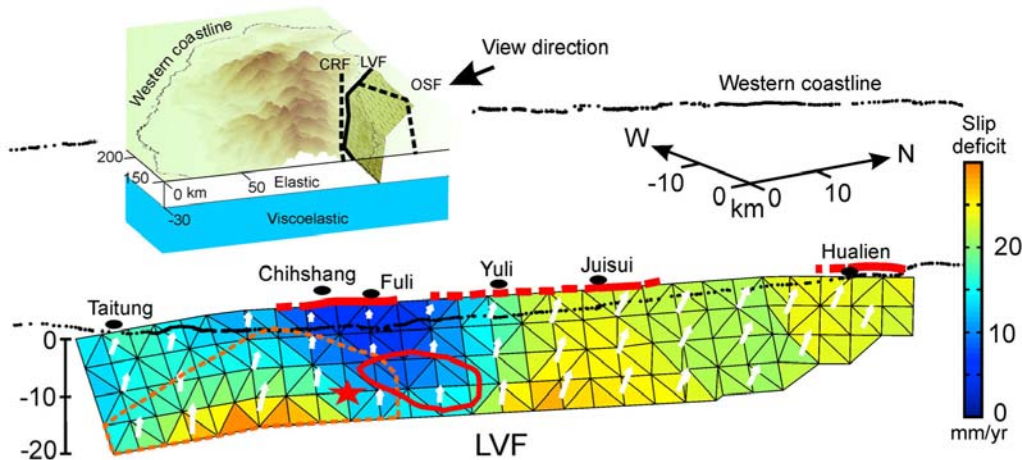


Figure 14. Slip deficit on LVF and the 1951 earthquake surface ruptures. The ruptures are shown with red lines [Hsu, 1962]. Projected hypocenter and approximate extent of coseismic slip of 2003 Chengkung earthquake (M_w 6.8) are shown as a red star and dashed orange polygon, respectively [Ching *et al.*, 2007]. Approximate extent of repeating earthquakes is shown as a red circle.

demonstrated that the total coseismic shift across a broad fault zone at the surface may be significantly larger than the slip at the surface trace [e.g., Johnson *et al.*, 2002; Rockwell *et al.*, 2002; Lienkaemper *et al.*, 2002]. Furthermore, coseismic slip at the ground surface may be less than slip at depth [e.g., Fialko *et al.*, 2005]. Lee *et al.* [2008] used the triangulation and GPS data to estimate the coseismic fault slip of 1951 earthquakes. Their inversion result shows the huge variation of coseismic fault slip along the fault strike from about 2.5 m in the south to about 20 m in the north.

[46] We point out that the two- and three-fault models predict not only different slip rates on the LVF, but different amounts of obliquity. The obliquity of slip on the LVF in the three-fault models is consistent with the obliquity of slip observed from surface ruptures of the 1951 earthquake sequence, while the two-fault model predicts nearly pure reverse slip. This is independent, although indirect, support of the conclusion that a significant amount of convergence is accommodated offshore on the OSF. The 1 April 2006, Taitung earthquake (M_w 6.1) occurred on the southern segment of the CRF 10 km in depth at 22.83°N and 121.06°E (its location shown in Figure 1) [Wu *et al.*, 2006]. According to Wu *et al.* [2006], the main shock and a number of aftershocks exhibited predominantly left-lateral slip. The hypocenter falls on our predicted locked segment of the southern CRF that shows oblique-reverse/left-lateral slip. As suggested by Wu *et al.* [2006], the oblique convergence may be partitioned in this region among near-vertical strike-slip faults and dipping reverse faults.

[47] The hypocenter and approximate extent of coseismic slip for the 2003 M_w 6.8 Chengkung earthquake is shown in Figure 14 [Kuo *et al.*, 2007; Ching *et al.*, 2007]. The earthquake nucleated near the boundary of the modeled creeping and locked regions and ruptured the modeled locked region south of Chengkung. Also shown is the approximate spatial extent of repeating earthquakes on the LVF [Ching *et al.*, 2007] which occur primarily in the modeled creeping region to the north of Chengkung. This setting appears to be analogous to the Parkfield, California segment of the San Andreas fault that produces $M \sim 6$

earthquakes at the boundary between locked and creeping sections of the fault and displays repeating earthquake sequences that may occur in creeping regions of the fault [e.g., Nadeau and McEvilly, 1999].

[48] It is incontrovertible that the LVF is an oblique reverse fault with sinistral motion. The southern segment of the LVF (south of Yuli, Figure 4) is largely accepted as an east dipping fault. However, there is conflicting evidence for the dip direction of northern segment of LVF. A number of scarplets on a northwest facing terrace along the western edge of the Coast Range near Hualien are consistent with a southeastward dip for the northern segment of the LVF [Hsu, 1955, 1962; Lin, 1957; Bonilla, 1975]. Consistent with this observation, the October 1951 earthquake produced 1.2 m of maximum uplift near Hualien on the southeast side of surface ruptures, again indicating a southeastward dip of the fault [Hsu, 1955, 1962; Lin, 1957; Bonilla, 1975]. In contrast, relocated earthquakes highlight a conspicuous northwest dipping zone (~ 20 km wide between 23°48' and 23°38') as shown by Kim *et al.* [2006] and K. H. Chen *et al.* [2007] showed a number of repeating earthquakes in this region that they interpreted as occurring in response to creep on a northwest dipping fault. In reality the system of faults in the vicinity of Hualien may be more complicated than in our model. We have modeled the LVF with an east dipping plane in this region for consistency with the geomorphic and 1951 earthquake observations.

[49] The Ryukyu trench system (Figure 1a) further complicates the fault geometry near Hualien. The geometry of faults in the offshore region where the Ryukyu trench merges with the Taiwan collision is unclear (see Shyu *et al.* [2005] for an interpretation). Therefore, it is difficult to know whether the inferred high interseismic creep rate on the northern segment of the OSF as shown in Figure 13c is real or a compensation for mismodeled fault geometry in this region. We find that this interseismic creep significantly improves the fit to the horizontal GPS velocities in the northern area of the Longitudinal Valley in comparison with models that do not allow this creep. For example, the

two-fault model (Figure 11a) does a poor job fitting horizontal GPS observations south of Hualien, but the fit is significantly improved if we include a dislocation to simulate the effect of interseismic locking of an interface at the Ryukyu trench. However, our experiments with models that include a fault to represent subduction at the Ryukyu trench offshore near Hualien show that interseismic locking of the subduction interface can also contribute to measured surface velocities near Hualien. Therefore, it is possible that our inference of creep on the northern OSF is biased by the lack of a contribution from locking of the subduction interface.

[50] Because the geometry of the CRF, LVF and OSF is not well known, we ran a number of inversions with different fault geometries to examine the influence of fault geometry on inversion results. We examined models with the CRF dipping over the range 45°, 65°, or 85°. The model with the CRF dipping 45° did not satisfactorily fit the data. The models with the CRF dipping 65° or 85° fit equally well with the CRF slip rates of about 12–13.5 mm/yr. The estimated slip rate of the CRF is largely controlled by the prior Gaussian probability distribution placed on this value. We considered models with the LVF dipping 40°, 50° or 60°. The models with the LVF dipping 40° or 60° systematically underpredict and overpredict, respectively, the coastal terrace uplift rates and so we reject these models. We considered models with the OSF dipping 25°, 30°, 35°, and 45°. The model with the OSF dipping 25° did not satisfactorily fit the data. The models with the OSF dipping 35° or 45° systematically underpredict the coastal terrace uplift rates. So, we reject these three models. We note that none of these runs showed distinct improvement to the misfit of the horizontal GPS velocities along the eastern coast. We suspect that the misfit is mainly due to more complicated geometry of LVF (such as listric-shaped) and/or OSF which we did not model.

8. Conclusions

[51] We demonstrate that the lithospheric block model is able to largely reproduce both horizontal and vertical interseismic and Holocene velocity patterns in eastern Taiwan. We invert geodetic and geologic data collected in eastern Taiwan for block movements, fault slip rates and distribution of interseismic creep and locked patches using the lithospheric lock model through a fully probabilistic inversion scheme. The best model for eastern Taiwan in this study includes four blocks separated by the Central Range fault, the Longitudinal Valley fault, and an offshore fault which is a west dipping thrust fault ~50 km east of eastern coast. The principle findings of the study are as follows: (1) Holocene uplift rates along eastern coast can only be reproduced if a significant amount of convergence is accommodated offshore on the OSF. (2) Measurements of interseismic deformation (GPS, InSAR, creepmeters) alone can be explained with either the two-fault or three-fault model; the Holocene uplift is required to distinguish between the two models. (3) Including the OSF in the model reduces the estimate of steady state slip rate on the LVF over Holocene by a factor of about two and changes the LVF from a nearly pure dip-slip reverse fault to an oblique reverse, left-lateral fault, consistent with independent observations. (4) The LVF is largely locked north of Yuli and is

creeping to the south. The transition from locked to creeping corresponds with the hypocenter of the 2003 Chengkung earthquake.

[52] The Holocene slip rate of the OSF is 35–55 mm/yr with the northern segment creeping interseismically at a high rate and the southern segment locked. We suggest that the high creep on the northern OSF may be a result of unmodeled effects of faulting associated with subduction at the Ryukyu trench. The Longitudinal Valley fault has a long-term slip rate of 20–30 mm/yr with approximately equal magnitudes of reverse-slip and left-lateral strike-slip components for the upper segment above the intersection with the OSF at about 20 km depth. The southern segment of the Longitudinal Valley fault creeps interseismically at a rate of 5–28 mm/yr. The maximum creep occurs between Fuli and Chihshang. The northern segment is mostly locked. The two places with maximum fault slip along two 1951 earthquake ruptures agree with the locations of high estimated slip deficit rate along the Longitudinal Valley fault. The slip rate and locking distribution of the Central Range fault are not well resolved by the inversion. The posterior distribution of the CRF slip rate is not significantly different from the prior distribution with mean rate of 12 mm/yr. The inferred distribution of creep on the CRF and OSF should be viewed with skepticism because of sparse data on the hanging wall side of the CRF and offshore.

[53] **Acknowledgment.** This work was supported by NSF grant EAR-0609620.

References

- Angelier, J., E. Barrier, and H. T. Chu (1986), Plate collision and paleostress trajectories in a fold-thrust belt: The foothills of Taiwan, *Tectonophysics*, 125, 161–178, doi:10.1016/0040-1951(86)90012-0.
- Angelier, J., H. T. Chu, and J. C. Lee (1997), Shear concentration in a collision zone: Kinematics of the Chihshang Fault as revealed by out-crop-scale quantification of active faulting, Longitudinal Valley, eastern Taiwan, *Tectonophysics*, 274, 117–143, doi:10.1016/S0040-1951(96)00301-0.
- Angelier, J., H. T. Chu, J. C. Lee, and J. C. Hu (2000), Active faulting and earthquake hazard: The case study of the Chihshang Fault, Taiwan, *J. Geodyn.*, 29, 151–185, doi:10.1016/S0264-3707(99)00045-9.
- Biq, C. C. (1972), Dual trench structure in the Taiwan-Luzon region, *Proc. Geol. Soc. China*, 15, 65–75.
- Bonilla, M. G. (1975), A review of recently active faults in Taiwan, *U.S. Geol. Surv. Open File Rep.*, 74-41, 58 pp.
- Bos, A. G., W. Spakman, and M. C. J. Nyst (2003), Surface deformation and tectonic setting of Taiwan inferred from a GPS velocity field, *J. Geophys. Res.*, 108(B10), 2458, doi:10.1029/2002JB002336.
- Chai, B. H. (1972), Structure and tectonic evolution of Taiwan, *Am. J. Sci.*, 272, 389–432.
- Chen, H., and R. Rau (2002), Earthquake locations and style of faulting in an active arc-continent plate boundary: The Chihshang fault of eastern Taiwan, *Eos Trans. AGU*, 83(47), Fall Meet. Suppl., Abstract T61B-1277.
- Chen, K. H., R. M. Nadeau, and R. J. Rau (2007), Towards a universal rule on the recurrence interval scaling of repeating earthquakes?, *Geophys. Res. Lett.*, 34, L16308, doi:10.1029/2007GL030554.
- Chen, W.-S., I.-C. Yen, K. P. Fengler, C.-M. Rulin, C.-C. Yang, H.-C. Cheng, C.-W. Lin, W.-H. Lin, Y.-C. Liu, and Y.-H. Lin (2007), Late Holocene paleoearthquake activity in the middle part of the Longitudinal Valley fault, eastern Taiwan, *Earth Planet. Sci. Lett.*, 264, 420–437, doi:10.1016/j.epsl.2007.09.043.
- Cheng, S.-N., Y. T. Yeh, and M.-S. Yu (1996), The 1951 Taitung earthquake in Taiwan, *J. Geol. Soc. China*, 39(3), 267–285.
- Ching, K.-E., R.-J. Rau, and Y.-H. Zeng (2007), Coseismic source model of the 2003 M_w 6.8 ChengKung earthquake, Taiwan, determined from GPS measurements, *J. Geophys. Res.*, 112, B06422, doi:10.1029/2006JB004439.
- Chuang, R. Y., M. Miller, J. B. H. Shyu, and Y. G. Chen (2008), Interseismic crustal deformation of Taiwan: An aspect of block tectonics,

- Geophys. Res. Abstr.*, 10, EGU 2008-A_03033, SRef-ID:1607-7962/gra/EGU2008-A-03033.
- Crespi, J. M., Y. C. Chan, and M. S. Swaim (1996), Synorogenic extension and exhumation of the Taiwan hinterland, *Geology*, 24, 247–250, doi:10.1130/0091-7613(1996)024<0247:SEAEOT>2.3.CO;2.
- Ding, Z. Y., Y. Yang, Z. Yao, and G. Zhang (2001), A thin-skinned collisional model for the Taiwan orogeny, *Tectonophysics*, 332, 321–331, doi:10.1016/S0040-1951(00)00289-4.
- Dominguez, S., J. Avouac, and R. Michel (2003), Horizontal coseismic deformation of the 1999 Chi-Chi earthquake measured from SPOT satellite images: Implications for the seismic cycle along the western foothills of central Taiwan, *J. Geophys. Res.*, 108(B2), 2083, doi:10.1029/2001JB000951.
- Feldl, N., and R. Bilham (2006), Great Himalayan earthquakes and the Tibetan Plateau, *Nature*, 444, 165–170, doi:10.1038/nature05199.
- Fialko, Y., D. Sandwell, M. Simons, and P. Rosen (2005), Three-dimensional deformation caused by the Bam, Iran, earthquake and the origin of shallow slip deficit, *Nature*, 435, 295–299, doi:10.1038/nature03425.
- Ho, C. S. (1986), A synthesis of the geologic evolution of Taiwan, *Tectonophysics*, 125, 1–16, doi:10.1016/0040-1951(86)90004-1.
- Hsieh, M.-L., P.-M. Liew, and M.-Y. Hsu (2004), Holocene tectonic uplift on the Hua-tung coast, eastern Taiwan, *Quat. Int.*, 115–116, 47–70, doi:10.1016/S1040-6182(03)00096-X.
- Hsu, L., and R. Bürgmann (2006), Surface creep along the Longitudinal Valley fault, Taiwan from InSAR measurements, *Geophys. Res. Lett.*, 33, L06312, doi:10.1029/2005GL024624.
- Hsu, T. L. (1955), The earthquakes of Taiwan (in Chinese), *Q. J. Bank Taiwan*, 7(2), 148–164.
- Hsu, T. L. (1962), Recent faulting in the Longitudinal Valley of eastern Taiwan, *Mem. Geol. Soc. China*, 1, 95–102.
- Hsu, T. L. (1976), Neotectonics of the Longitudinal Valley, eastern Taiwan, *Bull. Geol. Surv. Taiwan*, 25, 53–62.
- Hsu, Y.-J., M. Simons, S.-B. Yu, L.-C. Kuo, and H.-Y. Chen (2003), A two-dimensional dislocation model for interseismic deformation of the Taiwan mountain belt, *Earth Planet. Sci. Lett.*, 211, 287–294, doi:10.1016/S0012-821X(03)00203-6.
- Johnson, A. M., K. M. Johnson, J. Durdella, M. Sözen, and T. Gür (2002), An emendation of elastic rebound theory: Main rupture and adjacent belt of right-lateral distortion detected by viaduct at Kaynasli, Turkey 12 November 1999 Düzce earthquake, *J. Seismol.*, 6, 329–346, doi:10.1023/A:1020031324622.
- Johnson, K. M., P. Segall, and S. B. Yu (2005), A viscoelastic earthquake cycle model for Taiwan, *J. Geophys. Res.*, 110, B10404, doi:10.1029/2004JB003516.
- Kim, K. H., J. M. Chiu, J. Pujol, K. C. Chen, B. S. Huang, Y. H. Yeh, and P. Shen (2005), Three-dimensional Vp and Vs structural models associated with the active subduction and collision tectonics in the Taiwan region, *Geophys. J. Int.*, 162, 204–220, doi:10.1111/j.1365-246X.2005.02657.x.
- Kim, K. H., J. M. Chiu, J. Pujol, and K. C. Chen (2006), Polarity reversal of active plate boundary and elevated oceanic upper mantle beneath the collision suture in central eastern Taiwan, *Bull. Seismol. Soc. Am.*, 96(3), 796–806, doi:10.1785/0120050106.
- Kuothen, H., Y. M. Wu, C. H. Chang, J. C. Hu, and W. S. Chen (2004), Relocation of eastern Taiwan earthquakes and tectonic implications, *Terr. Atmos. Ocean.*, 15, 647–666.
- Kuothen, H., Y. M. Wu, Y. G. Chen, and R. Y. Chen (2007), 2003 M_w 6.8 Chengkung earthquake and its associated seismogenic structures, *J. Asian Earth Sci.*, 31, 332–339, doi:10.1016/j.jseae.2006.07.028.
- Lee, J. C., and J. Angelier (1993), Location of active deformation and geodetic data analyses: An example of the Longitudinal Valley fault, Taiwan, *Bull. Soc. Geol. Fr.*, 164(4), 533–570.
- Lee, J. C., J. Angelier, H. T. Chu, J. C. Hu, and F. S. Jeng (2001), Continuous monitoring of an active fault in a plate suture zone: A creepmeter study of Chihshang active fault, eastern Taiwan, *Tectonophysics*, 333, 219–240, doi:10.1016/S0040-1951(00)00276-6.
- Lee, J. C., J. Angelier, H. T. Chu, J. C. Hu, J. C. Hu, and F. S. Jeng (2005), Monitoring active fault creep as a tool in seismic hazard mitigation. Insights from creepmeter study at Chishang, Taiwan, *C. R. Geosci.*, 337(13), 1200–1207, doi:10.1016/j.crte.2005.04.018.
- Lee, Y. H., G. T. Chen, R. J. Rau, and K.-E. Ching (2008), Coseismic displacement and tectonic implication of 1951 Longitudinal Valley earthquake sequence, eastern Taiwan, *J. Geophys. Res.*, 113, B04305, doi:10.1029/2007JB005180.
- Lienkaemper, J. J., T. E. Dawson, S. F. Personius, G. G. Seitz, L. M. Reidy, and D. P. Schwartz (2002), A record of large earthquakes on the southern Hayward Fault for the past 500 years, *Bull. Seismol. Soc. Am.*, 92(7), 2637–2658, doi:10.1785/0120000611.
- Lin, C. C. (1957), *Geomorphology of Taiwan* (in Chinese), 421 pp., Taiwan Prov. Lit. Comm., Taipei.
- Loevenbruck, A., R. Cattin, X. Le Pichon, M.-L. Courty, and S.-B. Yu (2001), Seismic cycle in Taiwan derived from GPS measurements, *C. R. Acad. Sci.*, 333, 57–64.
- Lundberg, N. (2003), Surface processes in the accretionary prism south of Taiwan: Response to tectonic forcing and oceanic 'climate', *Geol. Soc. Am. Abstr. Programs*, 36(6), 29.
- Malavieille, J., S. E. Lallemand, S. Domingues, A. Deschamps, C. Y. Lu, C. S. Liu, and P. Schnürle (2002), Arc-continent collision in Taiwan: New Marine observations and tectonic evolution, *Spec. Pap. Geol. Soc. Am.*, 358, 187–211.
- McCaffrey, R. (2002), Crustal block rotations and plate coupling, in *Plate Boundary Zones, Geodyn. Ser.*, vol. 30, edited by S. Stein and J. Freymueller, pp. 101–122, AGU, Washington, D. C.
- Meade, B. J., and B. H. Hager (2005), Block models of present crustal motion in southern California constrained by GPS measurements, *J. Geophys. Res.*, 110, B03403, doi:10.1029/2004JB003209.
- Nadeau, R. M., and T. V. McEvilly (1999), Fault slip rates at depth from recurrence intervals of repeating microearthquakes, *Science*, 285, 718–721, doi:10.1126/science.285.5428.718.
- Rockwell, T. K., S. Lindvall, T. Dawson, R. Lanridge, W. Lettis, and Y. Klinger (2002), Lateral offsets on surveyed cultural features resulting from the 1999 Yzmit and Düzce earthquakes, Turkey, *Bull. Seismol. Soc. Am.*, 92(1), 79–94, doi:10.1785/0120000809.
- Savage, J. (1983), A dislocation model of strain accumulation and release at a subduction zone, *J. Geophys. Res.*, 88, 4984–4996, doi:10.1029/JB088iB06p04984.
- Savage, J., and W. Prescott (1978), Asthenosphere readjustment and the earthquake cycle, *J. Geophys. Res.*, 83, 3369–3376, doi:10.1029/JB083iB07p03369.
- Sella, G. F., T. H. Dixon, and A. Mao (2002), REVEL: A model for Recent plate velocities from space geodesy, *J. Geophys. Res.*, 107(B4), 2081, doi:10.1029/2000JB000033.
- Seno, T., S. Stein, and A. E. Gripp (1993), A model for the motion of the Philippine Sea Plate consistent with NUVEL-1 and geological data, *J. Geophys. Res.*, 98(B10), 17,941–17,948, doi:10.1029/93JB00782.
- Shyu, J. B. H., K. Sieh, Y.-G. Chen, and C.-S. Liu (2005), Neotectonic architecture of Taiwan and its implications for future large earthquakes, *J. Geophys. Res.*, 110, B08402, doi:10.1029/2004JB003251.
- Shyu, J. B. H., K. Sieh, J.-P. Avouac, W.-S. Chen, and Y.-G. Chen (2006a), Millennial slip rate of the Longitudinal Valley fault from river terraces: Implications for convergence across the active suture of eastern Taiwan, *J. Geophys. Res.*, 111, B08403, doi:10.1029/2005JB003971.
- Shyu, J. B. H., K. Sieh, Y.-G. Chen, and L.-H. Chung (2006b), Geomorphic analysis of the Central Range fault, the second major active structure of Longitudinal Valley suture, eastern Taiwan, *Bull. Seismol. Soc. Am.*, 118, 1447–1462, doi:10.1130/B25905.1.
- Simoes, M., and J. P. Avouac (2006), Investigating the kinematics of mountain building in Taiwan from the spatiotemporal evolution of the foreland basin and western foothills, *J. Geophys. Res.*, 111, B10401, doi:10.1029/2005JB004209.
- Simoes, M., J. P. Avouac, O. Beyssac, B. Goffé, K. A. Farley, and Y.-G. Chen (2007), Mountain building in Taiwan: A thermokinematic model, *J. Geophys. Res.*, 112, B11405, doi:10.1029/2006JB004824.
- Toussaint, G., E. Burov, and J. P. Avouac (2004), Tectonic evolution of a continental collision zone: A thermomechanical numerical model, *Tectonics*, 23, TC6003, doi:10.1029/2003TC001604.
- Tsai, Y. B. (1985), A study of disastrous earthquakes in Taiwan, 1683–1895, *Bull. Inst. Earth Sci. Acad. Sin.*, 5, 1–44.
- Vergne, J., R. Cattin, and J. P. Avouac (2001), On the use of dislocations to model interseismic strain and stress build-up at intracontinental thrust faults, *Geophys. J. Int.*, 147, 155–162, doi:10.1046/j.1365-246X.2001.00524.x.
- Wang, C., and W. Burnett (1990), Holocene mean uplift rates across an active plate-collision boundary in Taiwan, *Science*, 248, 204–206, doi:10.1126/science.248.4952.204.
- Willett, S. D., and M. T. Brandon (2002), On steady states in mountain belts, *Geology*, 30, 175–178, doi:10.1130/0091-7613(2002)030<0175:OSSIMB>2.0.CO;2.
- Wu, F. (1978), Recent tectonics in Taiwan, *J. Phys. Earth*, 26, Suppl., S265–S299.
- Wu, Y. M., Y. G. Chen, C. H. Chang, L. H. Chung, T. L. Teng, F. T. Wu, and C. F. Wu (2006), Seismogenic structure in a tectonic suture zone: With new constraints from 2006 M_w 6.1 Taitung earthquake, *Geophys. Res. Lett.*, 33, L22305, doi:10.1029/2006GL027572.
- Yu, S. B., and L. C. Kuo (2001), Present-day crustal motion along the longitudinal Valley fault, eastern Taiwan, *Tectonophysics*, 333, 199–217, doi:10.1016/S0040-1951(00)00275-4.
- Yu, S. B., and C. C. Liu (1989), Fault creep on the central segment of the longitudinal fault, eastern Taiwan, *Proc. Geol. Soc. China*, 32(3), 209–231.

- Yu, S.-B., D. D. Jackson, G.-K. Yu, and C.-C. Liu (1990), Dislocation model for crustal deformation in Longitudinal Valley area, eastern Taiwan, *Tectonophysics*, *183*, 97–109, doi:10.1016/0040-1951(90)90190-J.
- Yu, S.-B., H.-Y. Chen, and L.-C. Kuo (1997), Velocity field of GPS stations in the Taiwan area, *Tectonophysics*, *274*, 41–59, doi:10.1016/S0040-1951(96)00297-1.
- Yu, S.-B., L.-C. Kuo, R.-S. Punongbayan, and E. G. Ramos (1999), GPS observation of crustal motion in the Taiwan-Luzon region, *Geophys. Res. Lett.*, *26*, 923–926, doi:10.1029/1999GL900148.
-
- J. Fukuda, Earthquake Research Institute, University of Tokyo, 1-1-1 Yayoi, Bunkyo-ku, Tokyo 113-0032, Japan.
- W.-J. Huang and S.-B. Yu, Institute of Earth Sciences, Academia Sinica, 128 Academia Rd., Sec. 2, Taipei 11529, Taiwan. (huang22@earth.sinica.edu.tw)
- K. M. Johnson, Department of Geological Sciences, Indiana University, 1001 E. 10th St., Bloomington, IN 47405, USA.